Science Advances
AAAS

Supplementary Materials for

Structured silicon for revealing transient and integrated signal transductions in microbial systems

Xiang Gao*, Yuanwen Jiang, Yiliang Lin, Kyoung-Ho Kim, Yin Fang, Jaeseok Yi, Lingyuan Meng, Hoo-Cheol Lee, Zhiyue Lu, Owen Leddy, Rui Zhang, Qing Tu, Wei Feng, Vishnu Nair, Philip J. Griffin, Fengyuan Shi, Gajendra S. Shekhawat, Aaron R. Dinner, Hong-Gyu Park*, Bozhi Tian*

*Corresponding author. Email: btian@uchicago.edu (B.T.); hgpark@korea.ac.kr (H.-G.P.); gaoxiang6803@gmail.com (X.G.)

The PDF file includes:

Fig. S15. Finite element simulation of laser-induced transient thermal distribution and corresponding fluidic convective flows.
Fig. S16. Attracted bacterial cells experienced intracellular Ca^{2+} elevation right after light illumination.
Fig. S17. Si nanowire can induce a rapid calcium wave in the biofilm.
Fig. S18. Cellular automaton model of Ca^{2+} wave propagation.
Fig. S19. Si nanowire is critical to uncover the rapid calcium signaling in *B. subtilis* biofilm.
Fig. S20. Endogenous calcium-sensitive protein further confirms the calcium signaling within *B. subtilis* biofilms.
Fig. S21. Calcium propagation under different inhibitors.
Fig. S22. Si nanowires can activate calcium signaling in *P. aeruginosa* biofilms.
Fig. S23. Intercellular calcium communications can occur across microbial species.
Fig. S24. Simulation of the size-dependent temperature distributions from Si discs with different diameters.
Fig. S25. The photothermal effect of the Si disc is inversely related to the disc size.
Fig. S26. The final calcium distribution patterns are correlated to the spatial temperature gradients right after the laser stimulation.
Fig. S27. The final calcium distribution pattern can be stable for at least 5 min.
Fig. S28. LIVE/DEAD assays show the bacterial viabilities after laser illuminations on Si discs.
Fig. S29. The spatial temperature gradient is always peaked near the disc edge rather than the center.
Fig. S30. Experimental and simulation results from Si microplates with different geometries further confirm the correlation between calcium distribution pattern and spatial gradient of temperature.
Fig. S31. Calcium signaling in conjunction with convective flows can cause biofilm disruption.
Fig. S32. Sequentially increased laser stimulations, compared with directly applying high-power laser stimulation, are more efficient to mechanically break the biofilm.
Fig. S33. Nanoindentation shows that the laser stimulation could alter the biofilm modulus.
Fig. S34. Biofilms exhibit calcium-dependent mechanical properties, similar to alginate hydrogels that are ionically cross-linked by Ca^{2+}.
Fig. S35. Ca^{2+} distributions in a living biofilm can be controlled by custom-design Si patterns.
Fig. S36. Microfluidic system for cell attraction and single-layer biofilm stimulation experiments.
Fig. S37. Si nanowire can activate potassium, calcium, and membrane signaling in *B. subtilis* biofilms.
Legends for movies S1 to S4

Other Supplementary Material for this manuscript includes the following:

(available at advances.sciencemag.org/cgi/content/full/6/7/eaay2760/DC1)

Movie S1 (.mp4 format). Si nanowire can induce a rapid Ca^{2+} wave in *B. subtilis* biofilm.
Movie S2 (.mp4 format). Si nanowire induced Ca^{2+} signaling under inhibitor.
Movie S3 (.mp4 format). Large Si microdisc induced a bidirectional circular Ca^{2+} wave in *B. subtilis* biofilm.
Movie S4 (.mp4 format). Calcium signaling in conjunction with convective flows can cause biofilm disruption.

Table S1. Comparison between different intercellular communication modes in bacterial community.

Category	Mechanism of action	Duration of activation	Propagation speed	Observation condition	Physiological significance
Quorum sensing	Production, release, detection and response to extracellular signaling molecules	Hours	~ 0.1 to 0.5 µm/s	Natural (without physical simulation)	Symbiosis, motility, sporulation, biofilm formation
Ion channel mediated electrical signaling	Potassium wave propagation	Hours	~ 1 µm/s	Natural (without physical simulation)	Prolonged response to balance nutrients and growth
Ion channel mediated electrical signaling (this study)	Calcium wave propagation	Seconds	~ 8 µm/s	Evoked (photothermal stimulation)	Fast response to external stress to promote survival

Table S2. Strains and plasmids used in this study.

Strain	Note
B. subtilis NCIB 3610	Bacillus Genetic Stock Center
B. subtilis NCIB 3610 *amyE*:: *P*$_{xyl}$- *apoaequorin*	This study
E.coli DH5α	American Type Culture Collection
E.coli DH5α /pSY1064	This study
Pseudomonas aeruginosa P2	A gift from Dr. Olga Zaborina
E.coli MG1655	*E. coli* Genetic Stock Center
E.coli BW25113	*E. coli* Genetic Stock Center
Plasmid	
pSG1154	Bacillus Genetic Stock Center
pSY1064	A gift from Dr. Guoping Zhao
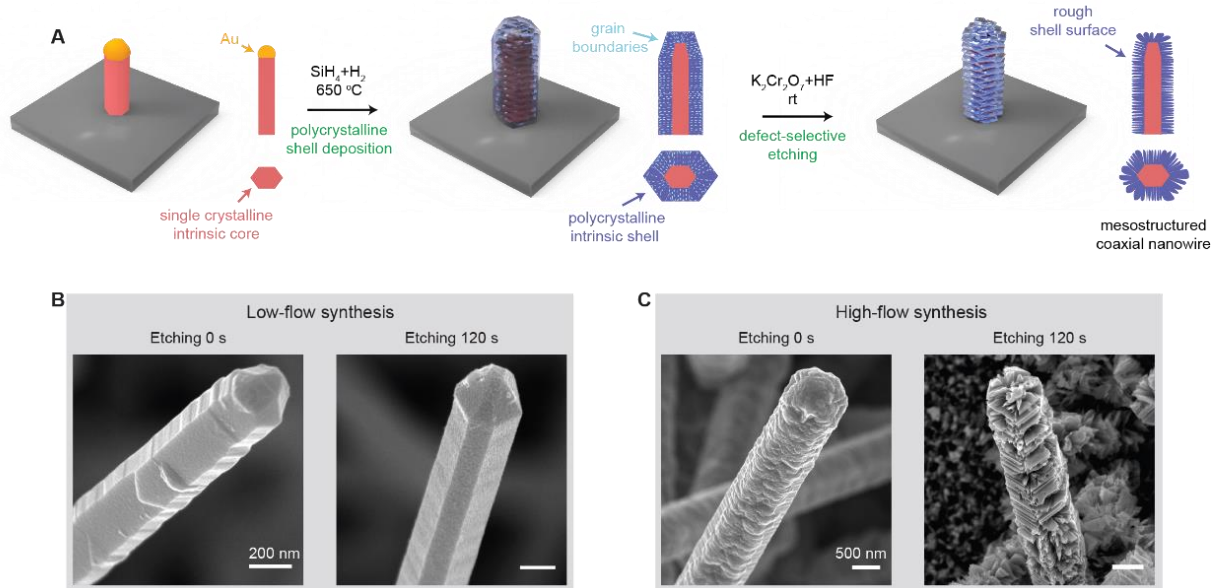
Fig. S1. Synthesis of *i-i* coaxial Si nanowires. (A) A schematic depicting the core-shell Si nanowire synthesis. Notably, mesostructured Si nanowires with rough and porous surface topographies can only be produced from defect-selective etching of Si after the high-flow synthesis since their number of grain boundaries are significantly higher than the low-flow ones (*i.e.,* there are fewer defects in the well-faceted shells during the thermodynamically-favored slow growth). **(B)** SEM images showing the surface structures of Si nanowires after the low-flow synthesis (SiH_4 and H_2 were delivered at 0.3 and 60 sccm, respectively) and after the defect selective etching (0.15 M $K_2Cr_2O_7$ and 49% HF (vol/vol=1/2) for 120 s at room temperature). Well faceted sidewalls can be produced after the low-flow condition and the etched nanowires are smooth and faceted. **(C)** SEM images showing the surface structures of Si nanowires after the high-flow synthesis (SiH_4 and H_2 were delivered at 1 and 60 sccm, respectively) and after the defect selective etching. The high-flow synthesis yielded rough surface topographies after growth and will be translated to the rough and porous mesostructures after the etching.
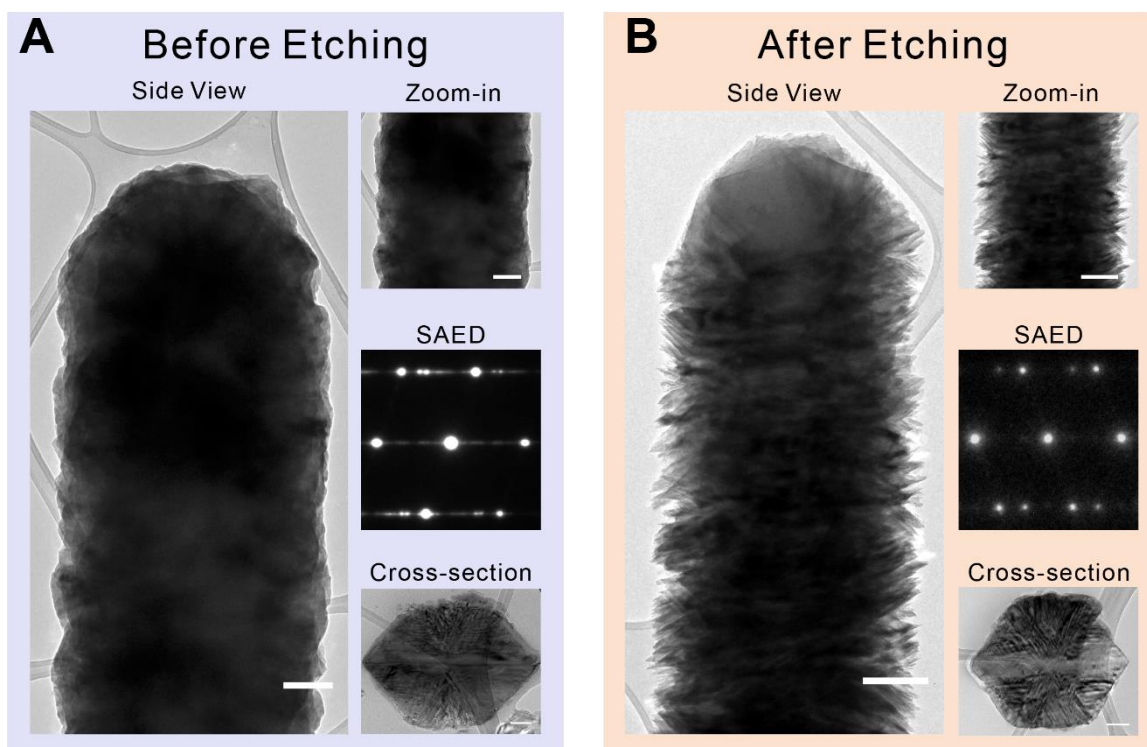
Fig. S2. TEM images of Si nanowires before and after defect-selective etching. Side-view TEM images and zoom-in views showing the relatively smooth and rough surfaces before (**A**) and after (**B**) etching. Corresponding selected area electron diffraction (SAED) patterns show an increased crystallinity after etching due to the removal of a substantial number of grain boundaries. Cross-sectional TEM images showed similar quasi-hexagonal shapes for both samples. Scale bars for side views and zoom-in views are 200 nm. Scale bar for cross-sectional views are 400 nm.
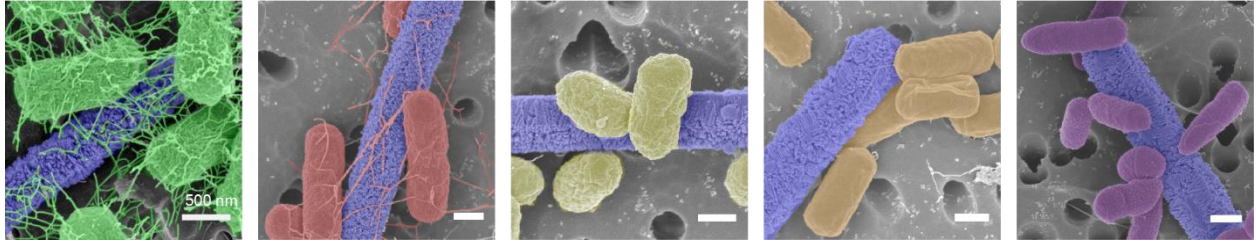
Fig. S3. Pseudocolored SEM images showing interactions between various bacterial cells and mesostructured nanowires. Blue: mesostructured nanowire; green: *E. coli* DH5α cells; red, *E. coli* MG1655 cells; yellow, *E. coli* BW25113 cells; orange, *B. subtiltis* cells; purple, *Pseudomonas aeruginosa* cells. Scale bars, 500 nm.

SYPRO Ruby Biofilm Matrix Stain   Phase contrast

15 µm   15 µm
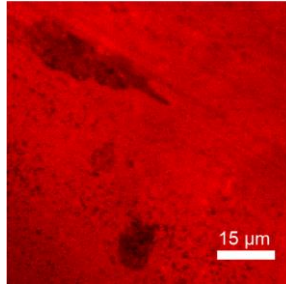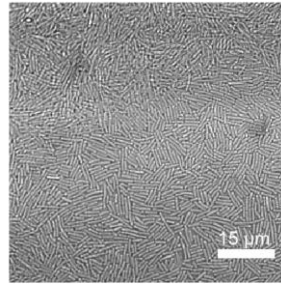
Fig. S4. A single-layer biofilm is consisting of a sheet of cells embedded in the extracellular matrix. The single layer biofilm was stained by the SYPRO Ruby assay and it confirms that most cells in the single layer biofilm were embedded with extracellular matrix.
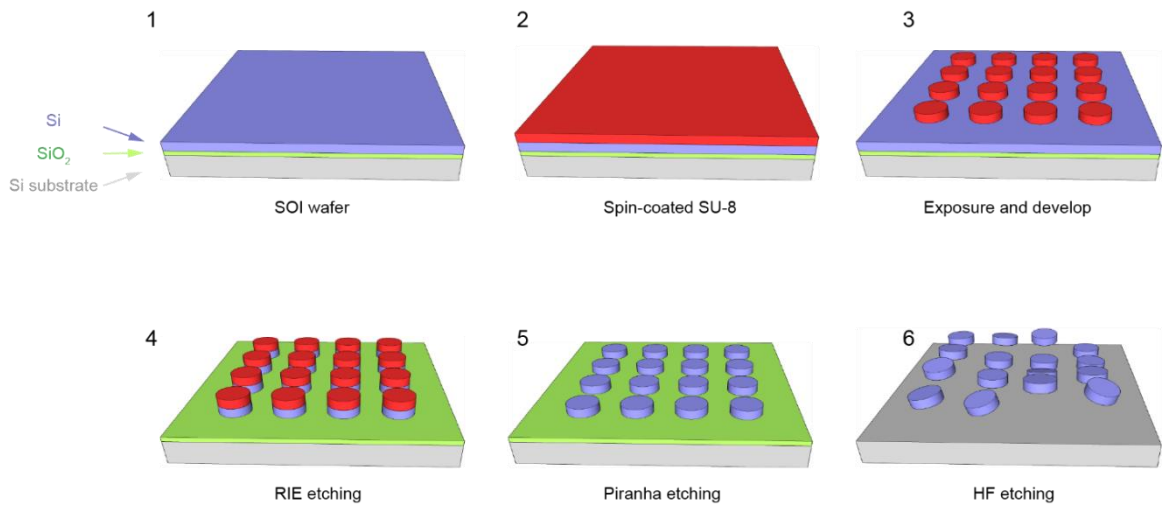
Fig. S5. Schematic illustration of the fabrication procedures for Si microplates. Fabrication of Si micro-plates with different shapes and sizes can be prepared by photolithography, reactive ion etching, and wet etching. The disc geometry is shown here as an example.
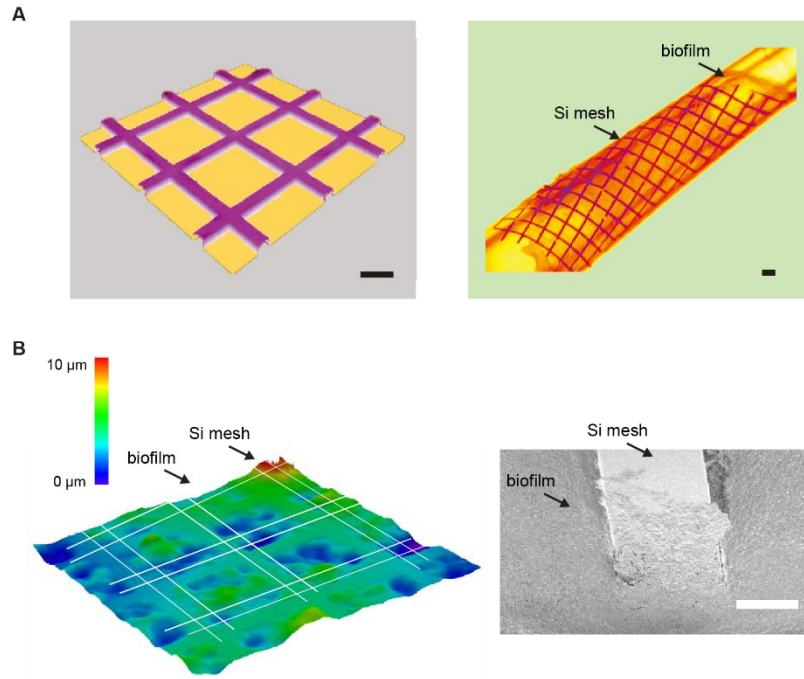
Fig. S6. Macroporous Si meshes can seamlessly integrate with biofilms. (A) 3D microscopy scan (left) of the grid structure from a Si mesh. Photograph (right) showing that the flexible Si mesh seamlessly integrates with a biofilm after co-culture. Scale bars, 100 µm. **(B)** A 3-D microscopy scan (left) of the biofilm cocultured with a Si mesh, the dashed lines represent the outline of the Si meshes. A SEM image (right) showing the interpenetrating nature of the Si/biofilm interface. Scale bar, 30 µm.
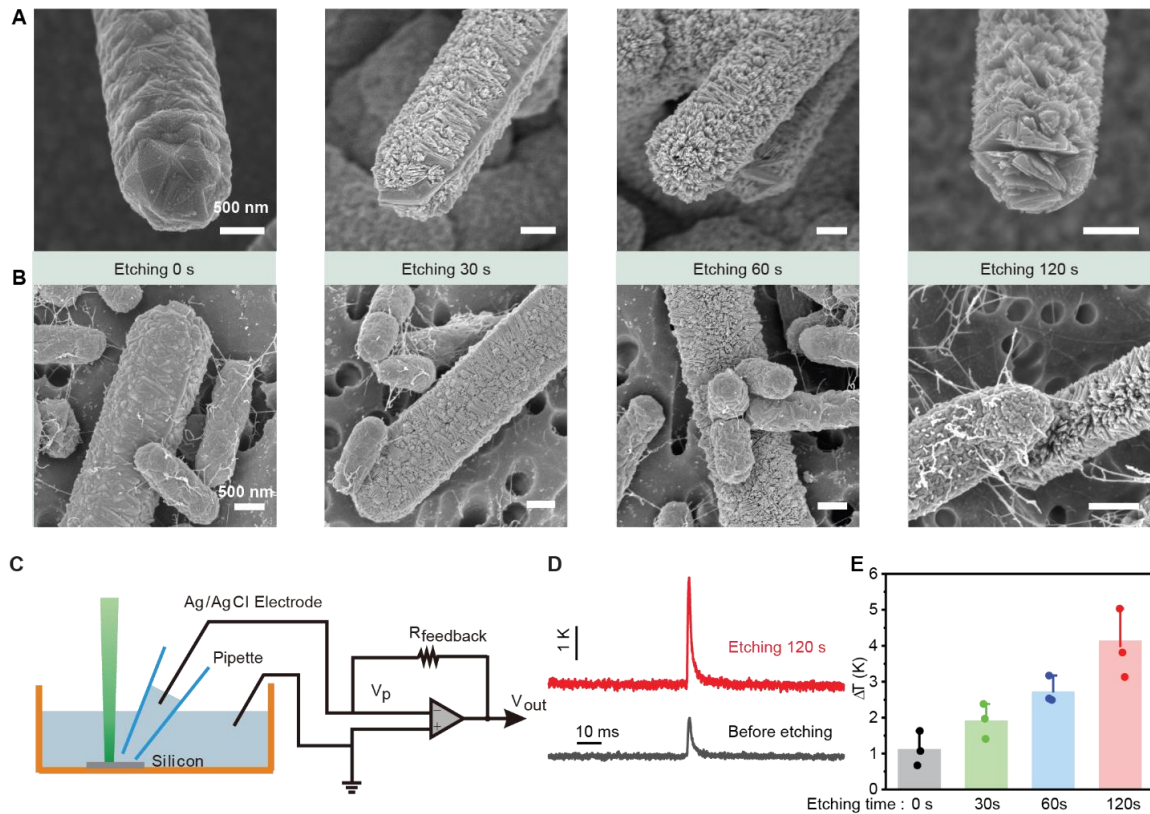
Fig. S7. The effect of Si nanowire mesostructures on the photothermal effect and interaction with bacteria. (**A**) SEM images of nanowires (from the high-flow synthesis) after being etched for 0 s, 30 s, 60 s, and 120 s, respectively. The roughness of the Si nanowire surfaces were highly dependent on the etching time. (**B**) SEM images showing interactions between *E. coli* cells and nanowires with different etching conditions. (**C**) A schematic diagram of the experimental setup for the photoresponse measurement of Si nanowires. 532 nm laser pulses were delivered onto the Si nanowires immersed in a PBS solution. (**D**) Representative traces of local temperature dynamics after laser illuminations (532 nm, 61.4 mW for 1 ms) of Si nanowires before etching (grey) and after 120 s of wet etching (red). (**E**) Si nanowires etched for longer time displayed increased photothermal effect. Longer etching time generated more cavities, which not only promoted light absorption, but also reduced the thermal conductivity for an enhanced photothermal effect. Three nanowires were measured for each group with 15 repetitive measurements per nanowire.
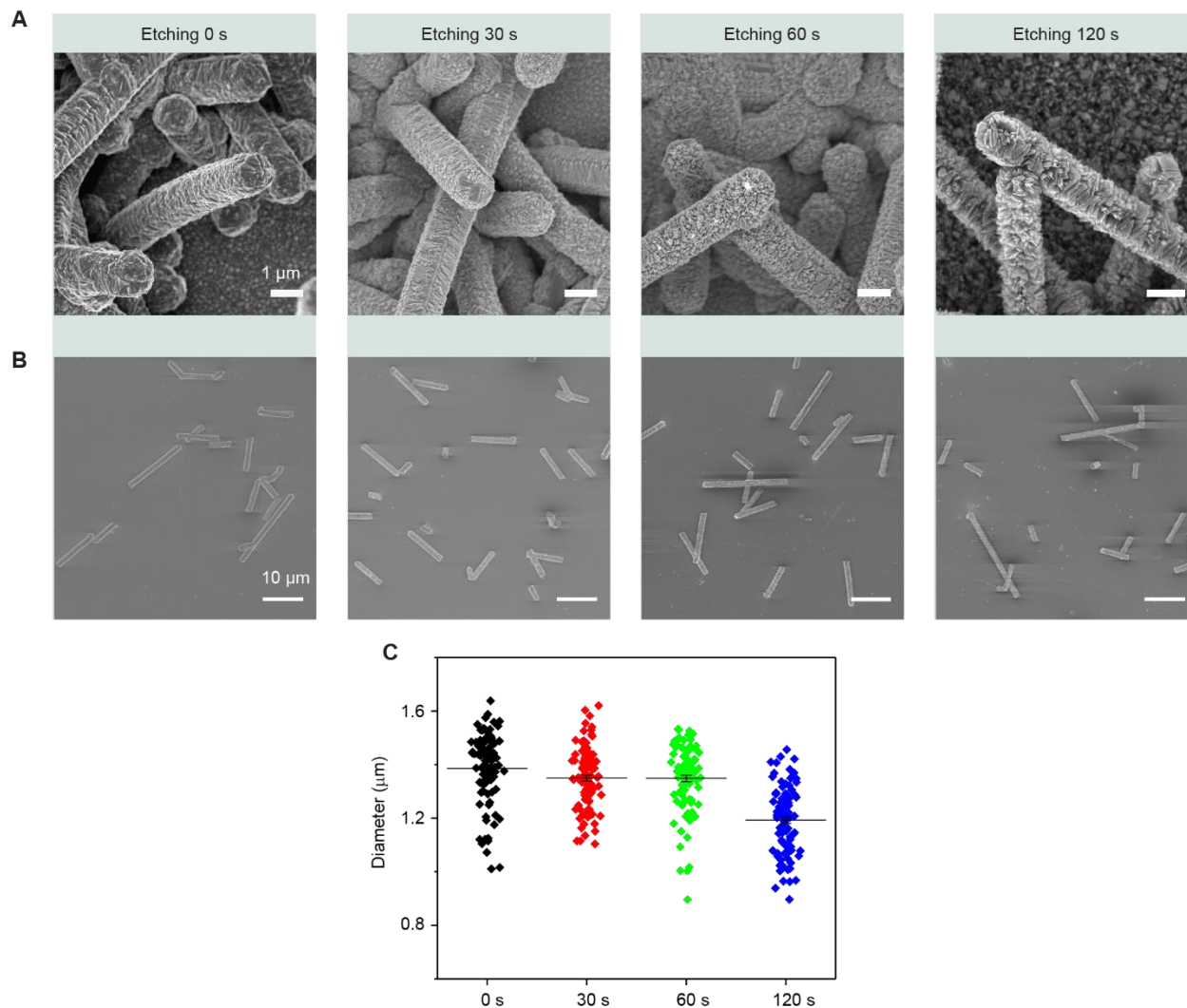
Fig. S8. SEM images showing the nanowires have pretty uniform surface roughness and diameter with different etching conditions. (**A**) Zoomed-in SEM images of nanowires after etching for 0 s, 30 s, 60 s, and 120 s, respectively. The surface roughness of nanowires in each condition are relatively uniform. (**B**) Low magnification SEM images of nanowires lying on flat substrates to show the uniformity in diameter. (**C**) Quantitative analysis of the nanowire diamters after different etching conditions. 100 nanowires from each etch condition were measured.

A

$$\rho c_p \frac{\partial T}{\partial t} + \rho c_p \mathbf{u} \nabla T - \kappa \nabla^2 T = \alpha Q$$

B

C

D
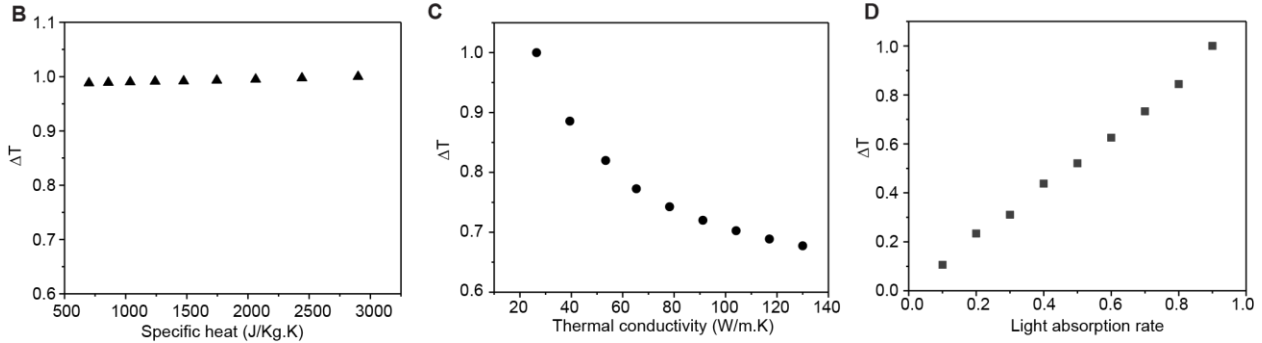
Fig. S9. Effects of specific heat, thermal conductivity, and light absorption on the nanowire photothermal response. Fourier thermal conduction equation and corresponding finite element simulation showing the relationship between light absorption rate (α), thermal conductivity (κ), and specific heat (c_p). ρ is the density of silicon, $\mathbf{u}$ is the flow velocity, Q is the input light energy. The results suggest reduced thermal conductivity and increased light absorption will lead to enhance photothermal response in the mesostructured nanowires. Specific heat does not change the photothermal effect significantly.
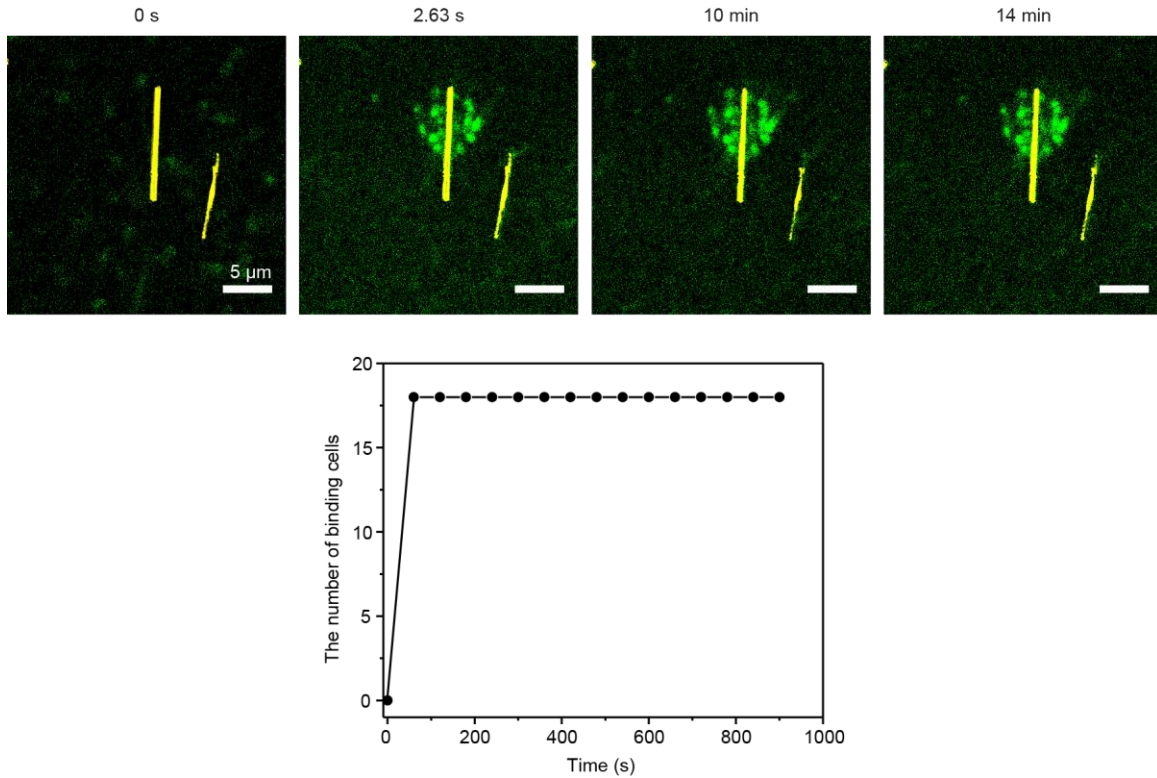
**Fig. S10. Nanowire attracted bacteria right after light illumination, and the binding interface can be stable for more than 10 mins.** The planktonic *B. subtilis* cells were illuminated by a Si nanowire with a laser pulse (592 nm, ~8.28 mW, ~500 nm spot size, 1 ms). The cells attracted to nanowire immediately after light illumination. The number of cells binding to the nanowire is plotted over time.
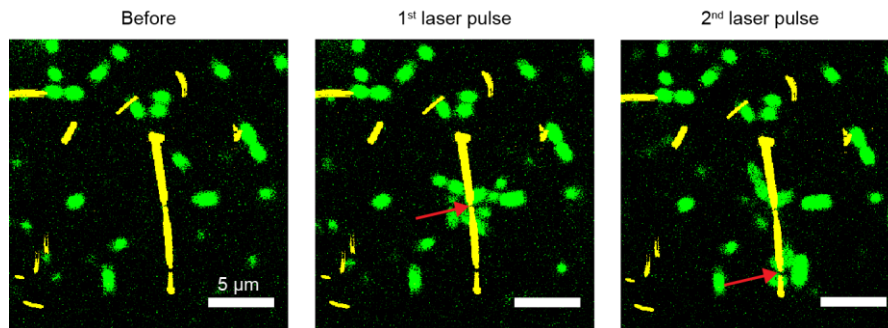
Fig. S11. Bacteria can relocate on the same Si nanowire after sweeping the laser spot. Bacterial cells can be attracted to the nanowire near the first laser spot (592 nm, 1 ms). After the second laser illumination on another location, some cells were relocated.
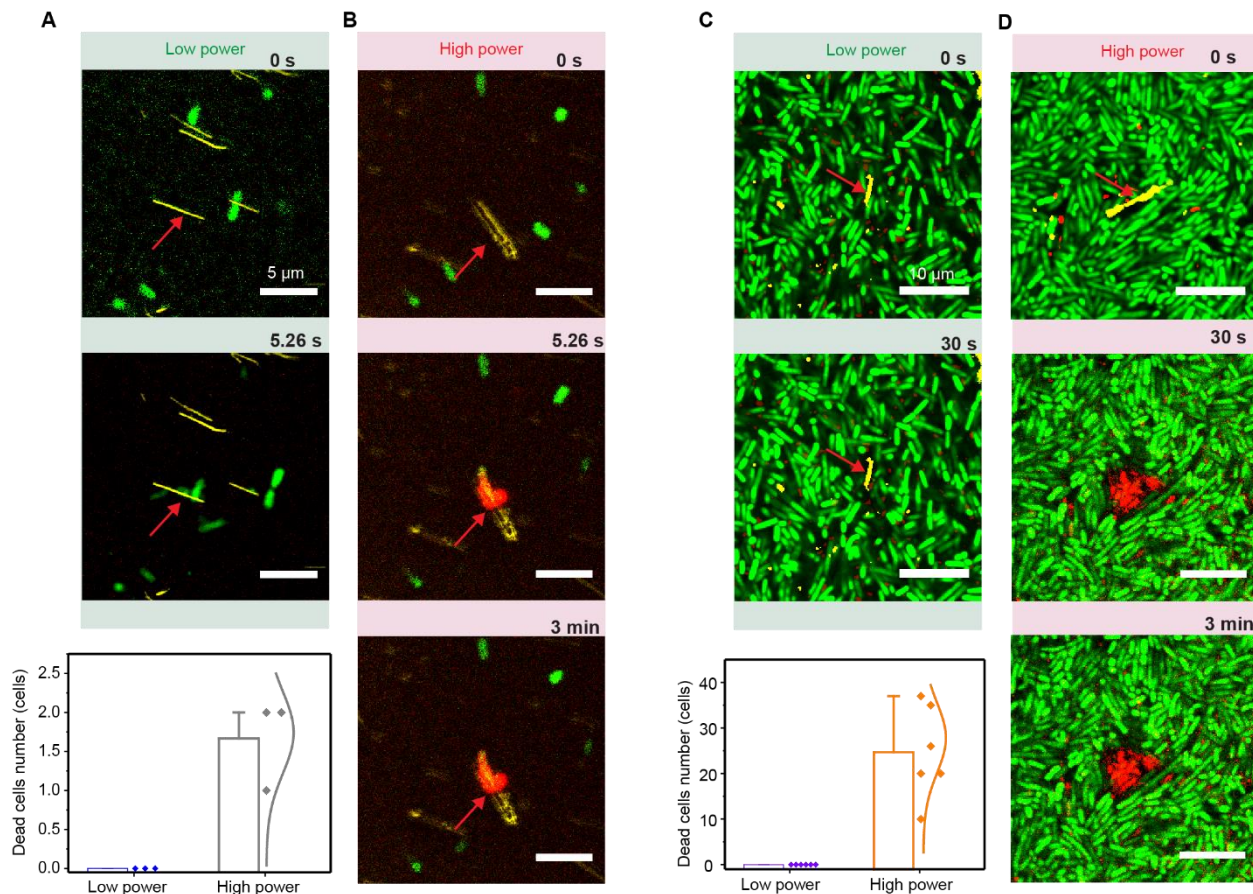
Fig. S12. LIVE/DEAD assays show the bacterial viability after laser illumination of single Si nanowires. (A) and **(B)**, Confocal images showing that *B. subtilis* cells were still alive after being attracted to the nanowires from a low-power laser stimulation (1-ms pulse of ~ 4.73 mW). With a high power stimulation (1-ms pulse of ~ 44.3 mW), cells can be killed. Quantitative analyses of number of dead cells after both low- and high-power stimulations are provided. **(C)** and **(D)**, Confocal images of biofilms showing that bacteria around the nanowire were still alive after the lower power illumination (~ 22.3 mW, 1 ms). High power (~ 182.0 mW, 1 ms) illumination will kill the nearby cells and even kick away the nanowire. Quantitative analyses of number of dead cells after both low- and high-power stimulations are provided.
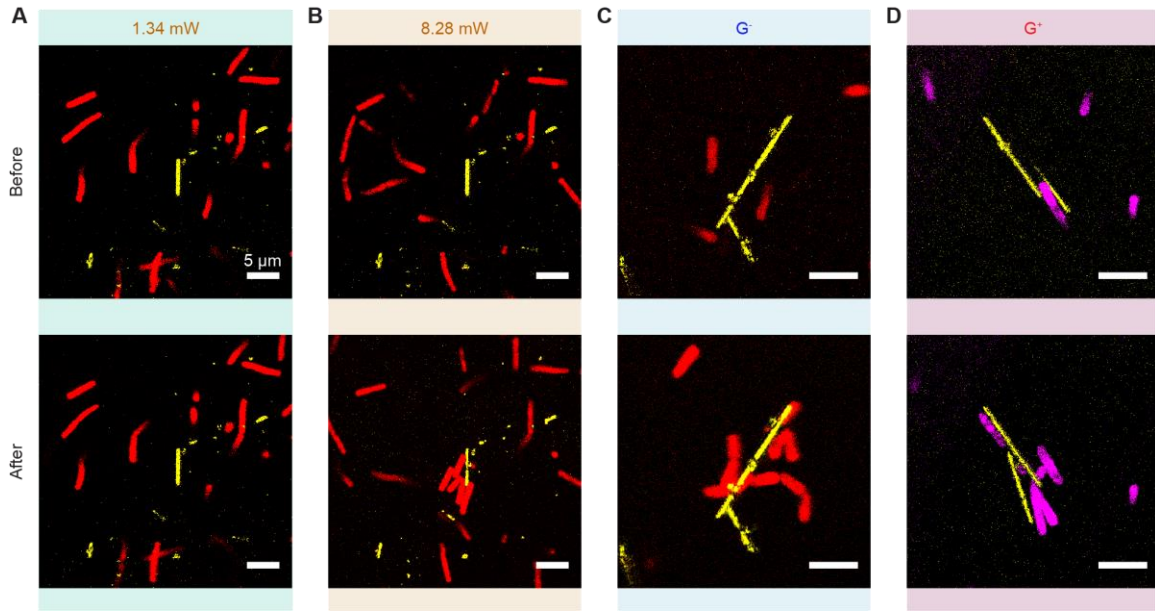
Fig. S13. Laser power determines the number of cells being attracted to the Si nanowires, regardless of the bacterial species. A and **B,** Confocal images showing that the bacterial attraction was laser-power dependent. While a low-power illumination of 1.34 mW (592 nm, 1 ms) on the Si nanowire (yellow) is not sufficient to attract *E.coli* cells expressing afred fluorescence protein (red), high power illumination (8.28 mW, 592 nm, 1 ms) can effective attract bacterial cells. **C** and **D**, Both gram negative strain (G⁻, *E.coli*, red in **C**) and positive strain (G⁺, *B. subtilis*, purple in **D**) bacteria can be attracted to the nanowire after illuminating a laser pulse (8.28 mW, 592 nm, 1 ms) on the Si nanowires.
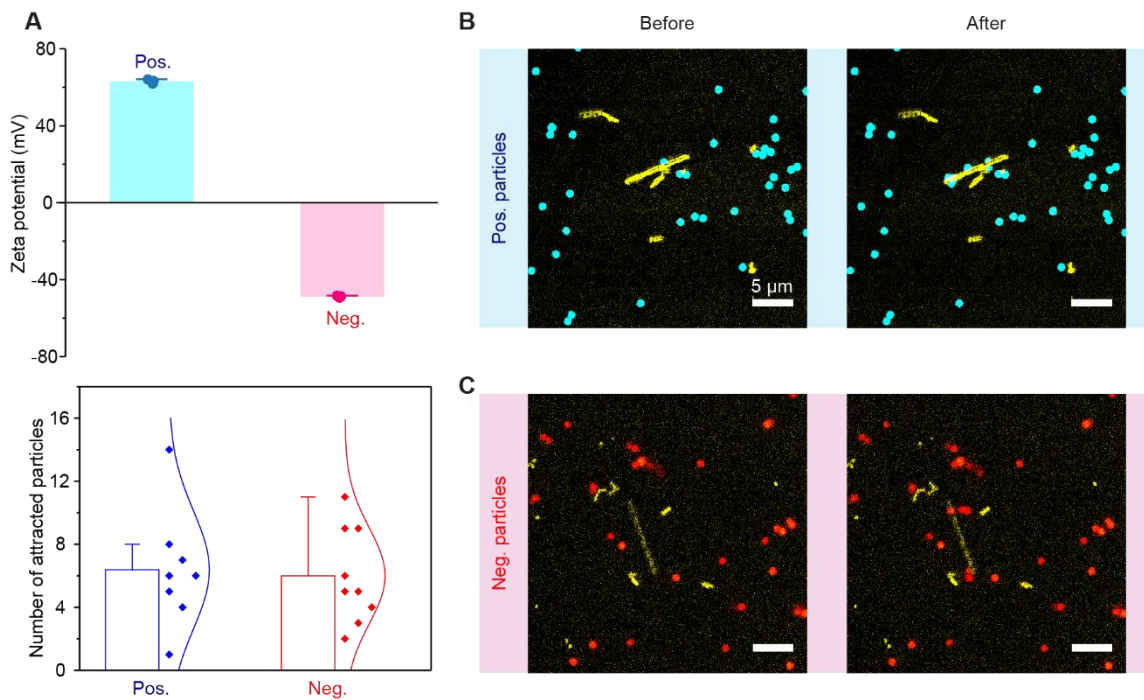
Fig. S14. Nanoparticles can be attracted to the Si nanowires, regardless of the surface charges.
(A) Zeta potentials (upper) of amine-terminated (blue; diameter, ~ 0.81 µm) and carboxyl-terminated polystyrene nanoparticles (red; diameter, ~ 0.84 µm). The number of particles being attracted after laser illumination is not dependent on their surface charges (bottom). **(B)** and **(C),** Laser illumination (592 nm, ~ 8.28 mW) could attract both positively-charged (blue) and negatively-charged nanoparticles (red). This suggests that the electrostatic interaction was not the major driving force for particles attraction. Particle densities were not controlled in this experiment.
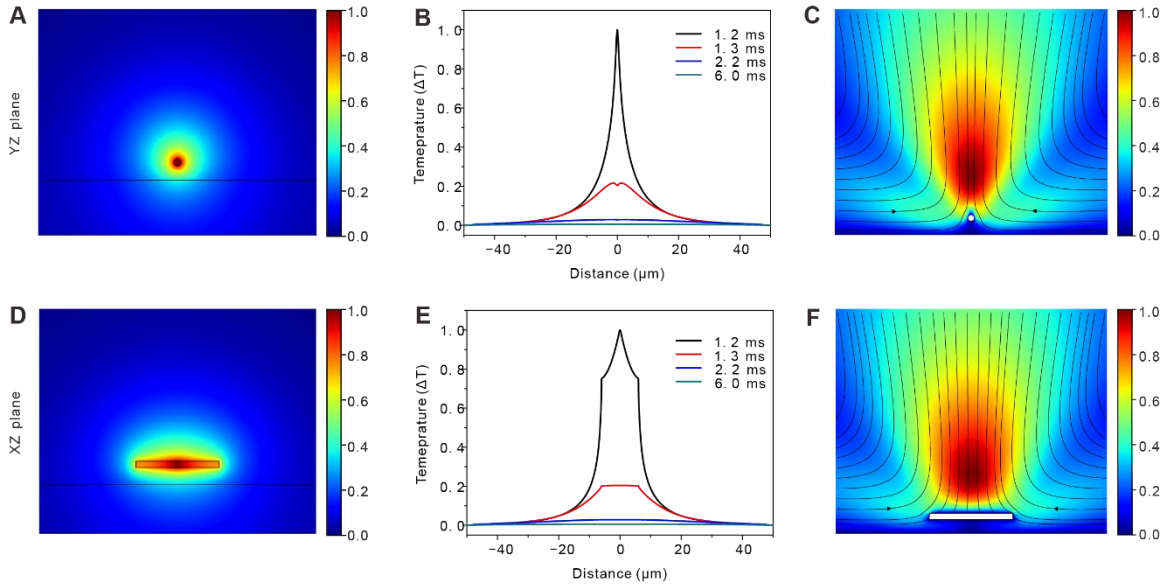
Fig. S15. Finite element simulation of laser-induced transient thermal distribution and corresponding fluidic convective flows. In the simulation, the 12-µm long Si nanowire (450 nm radius) aligned with the *x*-axis was placed in water at the distance of 2 µm above the glass substrate. The laser-induced heat was applied at the center of the nanowire with the heat density of 13.5 mW/µm³, corresponding to the laser power of 8.14 mW. **(A)** and **(B),** Distribution of normalized temperature change, *ΔT*, near the Si nanowire in the **(A)** *yz*-plane and **(D)** *xz*-plane at the time point of 1.2 ms. **(B)** and **(E),** *ΔT* profile at the top of the nanowire from different time points of 1.2, 1.3, 2.2 and 6.0 ms in the **(B)** *y*-direction and **(E)** *x*-direction. After the laser was turned off, locally generated heat in the nanowire was effectively transferred to water by convection as well as conduction. As a result, the temperature at the top of the nanowire would gradually decrease. **(C)** and **(F),** Normalized water flow velocity distribution near the nanowire. The maps show the magnitudes of the flow velocity and the stream lines show the flow direction in the **(c)** *yz*-plane and **(F)** *xz*-plane at the time point of 1.2 ms. The vertical convective water flow was generated by the laser-induced heat in the nanowire, and as a result, the convective fluidic flows towards nanowire were observed.
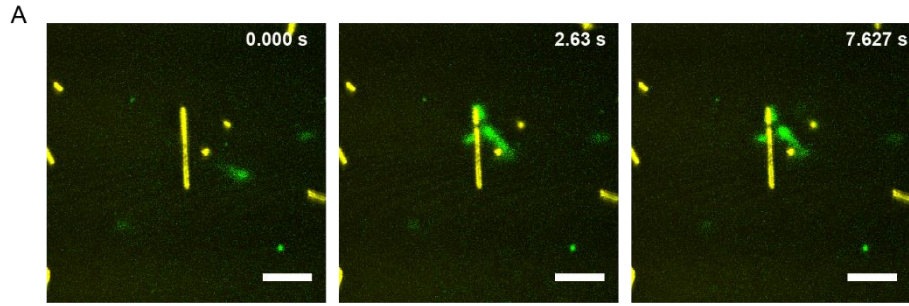
Fig. S16. Attracted bacterial cells experienced intracellular Ca²⁺ elevation right after light illumination. The stained planktonic *B. subtilis* cells with a calcium indicator (*i.e.,* Fluo-4 acetyloxymethyl ester) and illuminated a nanowire with a laser pulse (592 nm, ~8.28 mW, ~500 nm spot size, 1 ms). The cells attracted to wire and increased intracellular Ca²⁺ fluorescence intensity immediately after light illumination.
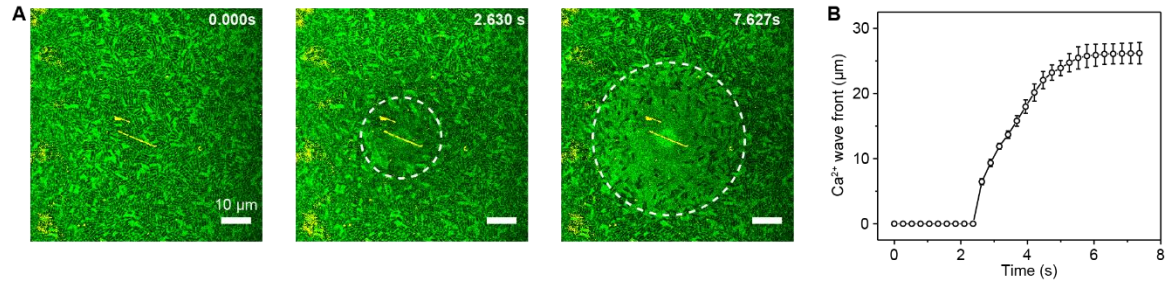
Fig. S17. Si nanowire can induce a rapid calcium wave in the biofilm. (A) Confocal microscope time series images show a calcium signaling propagation from the simulation spot. The laser illumination (592 nm, ~ 22.3 mW) was on for 1 ms right before the time point 2.630 s. **(B)** Quantitative analysis of the location of calcium wave front from the illumination spot during the propagation.
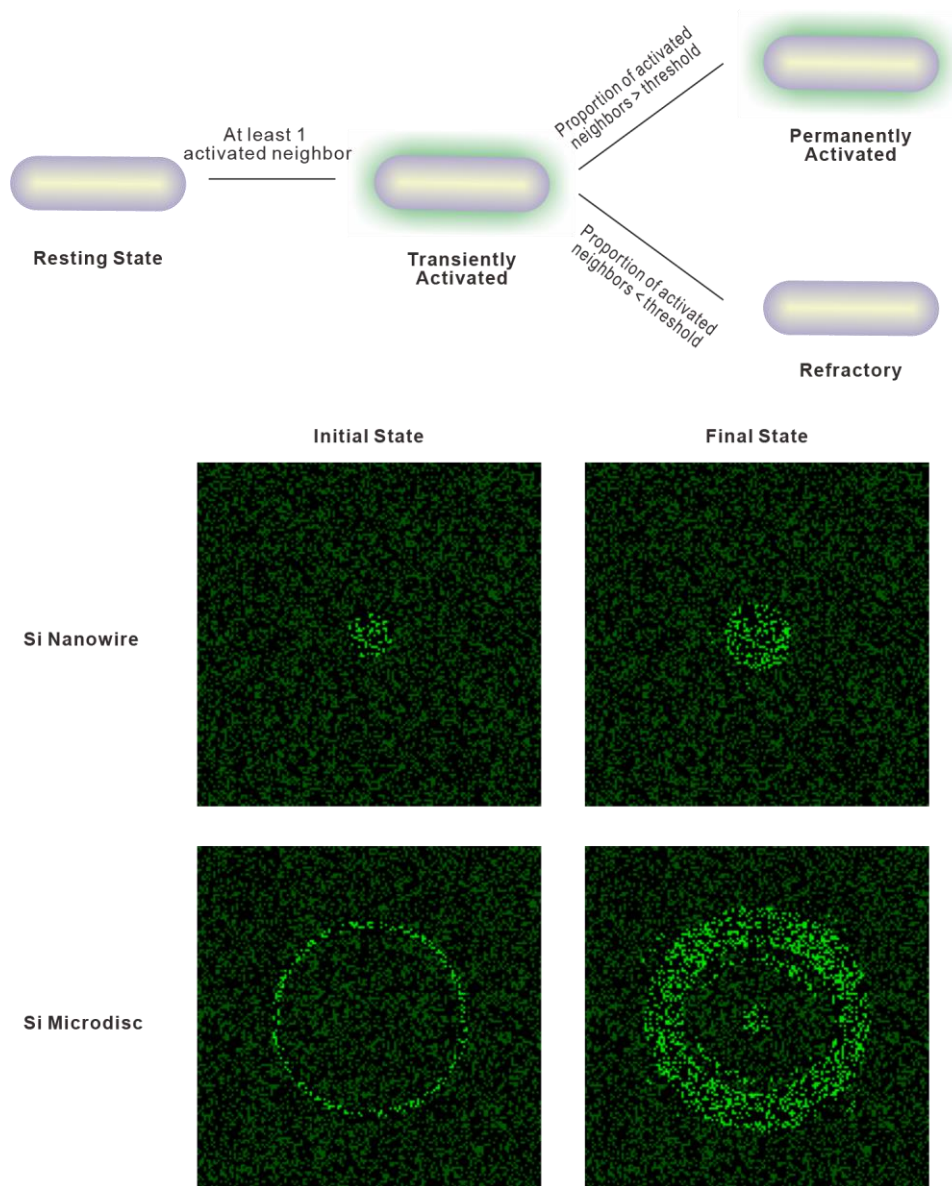
Fig. S18. Cellular automaton model of Ca²⁺ wave propagation. A simple, discrete model of calcium signaling. **Upper,** State transition rules for the cellular automaton. Each transition occurs over 1 discrete time step. **Lower,** when run on a graph of randomly distributed nodes representing cells, the model qualitatively reproduces the limited propagation of the activated region observed when the biofilm is stimulated using a Si nanowire, as well as the activated central spot of high calcium that appears when the biofilm stimulated by a Si disc.
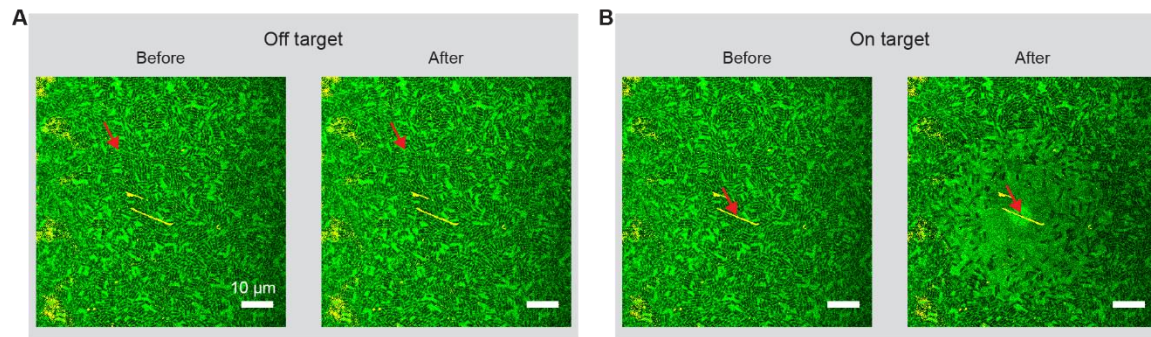
Fig. S19. Si nanowire is critical to uncover the rapid calcium signaling in *B. subtilis* biofilm.
(A) Direct laser illumination on the cells cannot activate calcium signaling even under a high laser power (~ 131.7 mW, 1 ms, 592 nm). **(B)** A low-power (~ 22.3 mW, 1 ms, 592 nm) stimulation on a nanowire can effectively induce a calcium wave. Taken together, without Si nanowires, it would be difficult to uncover the new mode of bacterial calcium signaling in our study. Red arrows indicate the laser spot positions.
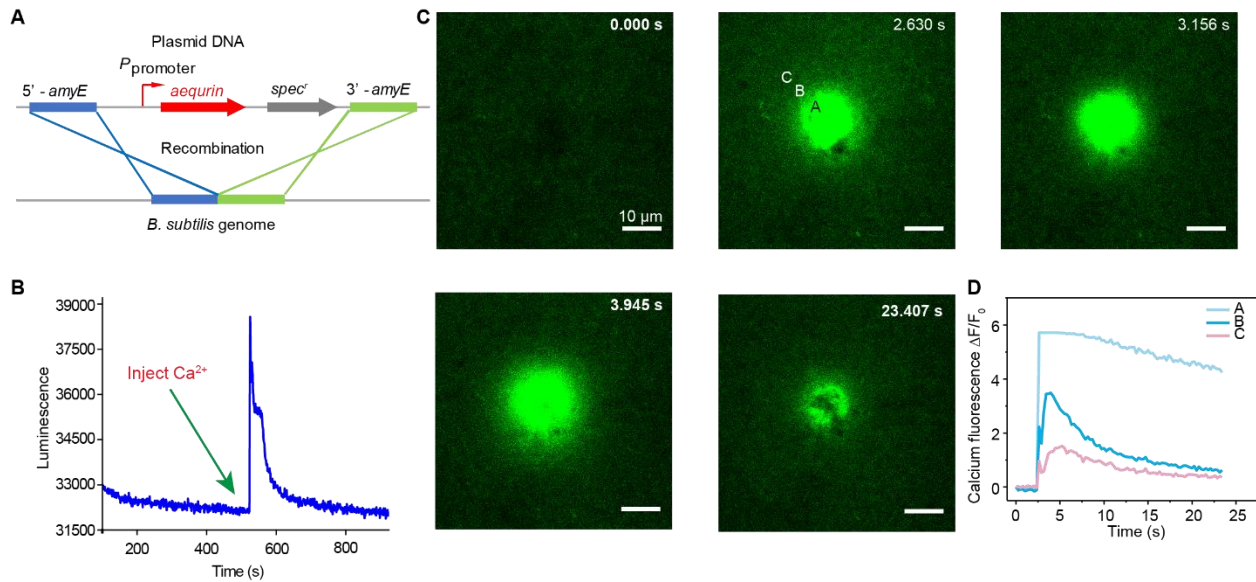
**Fig. S20. Endogenous calcium-sensitive protein further confirms the calcium signaling within *B. subtilis* biofilms. (A)** A schematic representation of the recombination that integrates the *aequrin* gene to the *amyE* locus of the *B. subtilis* chromosome. **(B)** *Aequrin* luminescence responds to exogenous calcium rapidly. Externally added 1 mM of Ca^{2+} induced a transient burst of intracellular Ca^{2+}, followed by a slower decay. **(C)** Confocal microscope time series images showing the calcium signaling propagation from the simulation spot (red arrow). The laser illumination (592 nm, ~ 54.1 mW) was on for 1 ms right before the time point 2.630 s. **(D)** Quantitative analysis of the Ca^{2+}fluorescence intensity over time showing the immediate Ca^{2+} activation near the laser spot and a delayed onset at the distal sites. Like a dye-based calcium indicator (*i.e.,* Fluo-4 AM), the endogenous calcium-sensitive protein also recorded the calcium signaling right after laser stimulation. This rule out the possibility that the observed fluorescence change was merely due to the transport of the calcium indicators.
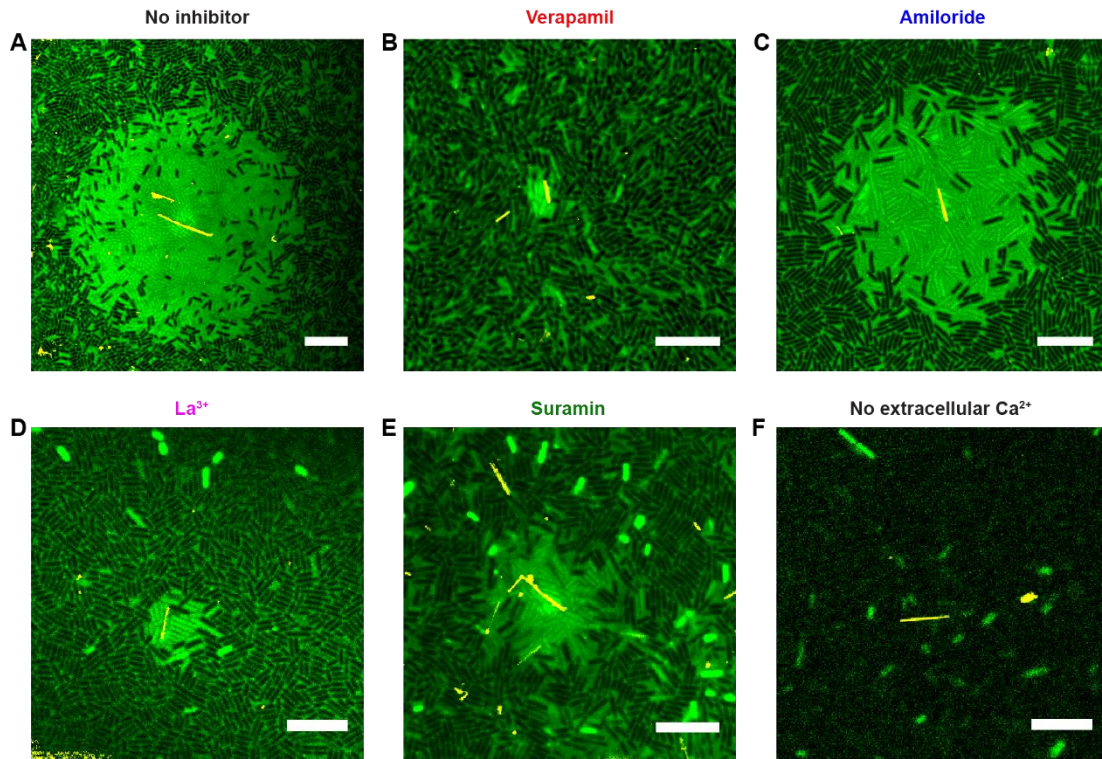
Fig. S21. Calcium propagation under different inhibitors. Calcium fluorescence images after laser stimulations on the Si nanowires with different inhibitors. Control groups, no inhibitor (**A**); 100 µM verapamil (**B**); 100 µM amiloride (**C**); 5 mM La^{3+} (**D**); 100 µM suramin (**E**); modified Msgg medium without extracellular calcium ion (**F**). Scale bar, 10 µm.
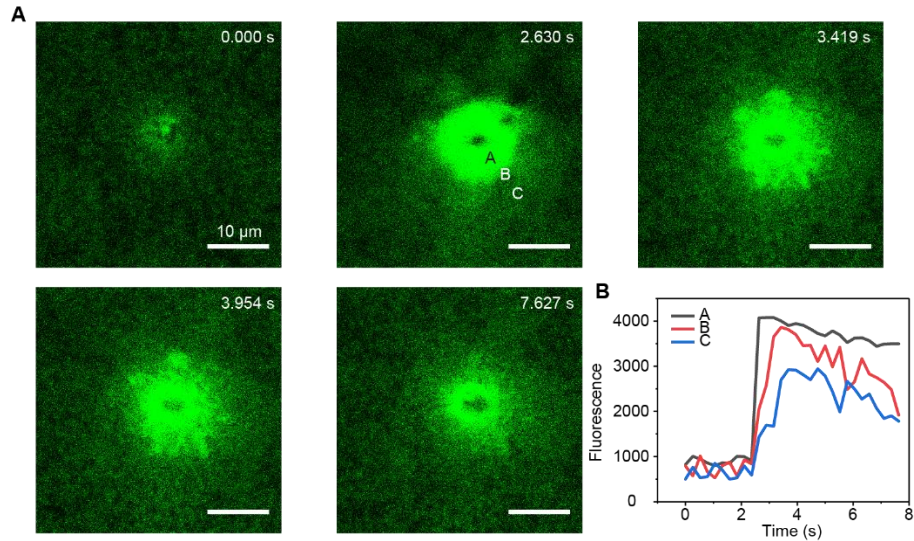
Fig. S22. Si nanowires can activate calcium signaling in *Pseudomonas aeruginosa* biofilms.
(A) Confocal microscope time series images showing a calcium signal propagation from the simulation spot (red arrow). The laser illumination (592 nm, ~ 54.1 mW) was on for 1 ms right before the time point 2.630 s. **(B)** Quantitative analysis of the Ca^{2+} fluorescence intensity over time showing the Ca^{2+} propagation over time. Since the laser-induced photothermal effect is simply a physical process, it should be able to stimulate calcium signaling in biofilms regardless of species. The biofilm was stained with Fluo-4 AM (green).
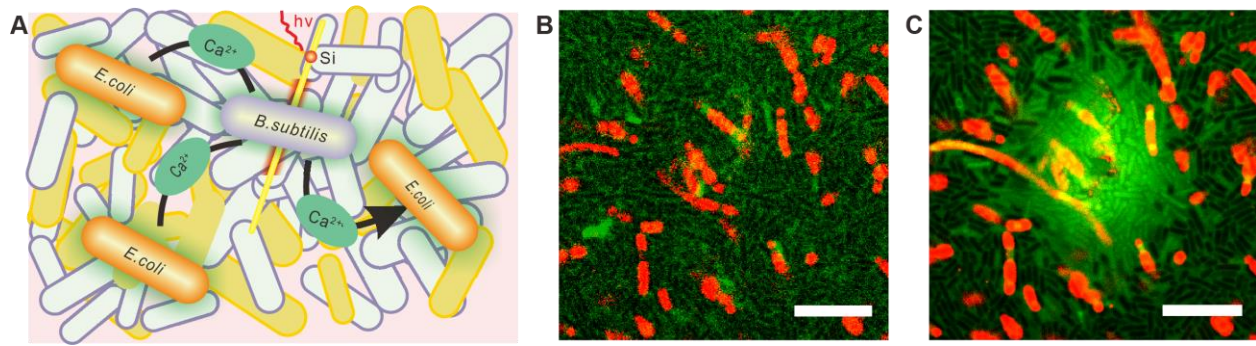
Fig. S23. Intercellular calcium communications can occur across microbial species. (A) Schematic illustration of the laser-induced calcium signaling propagating from the *B.subtilis* cells to the neighboring *B. subtilis* cells and *E. coli* cells. **(B)** and **(C)**, Confocal microscope images of calcium signals before (**B**) and after (**C**) laser stimulation (592 nm, 1 ms, ~32.2 mW). The results showed that the activated *B. subtilis* cells can propagate calcium signals not only to the neighboring *B. subtilis* cells (green), but also *E. coli* cells (red), suggesting that the intercellular calcium communication is universal across different microbial species. Scale bar, 10 µm.
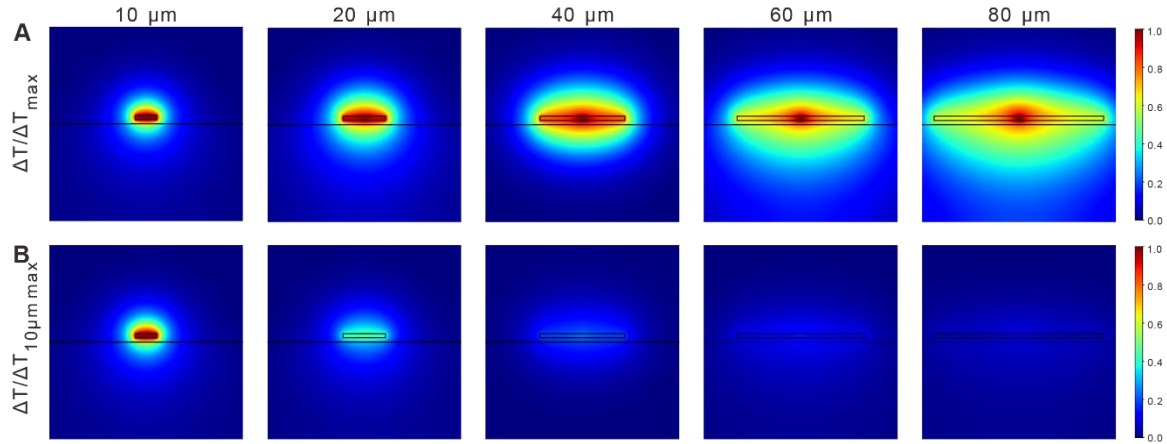
Fig. S24. Simulation of the size-dependent temperature distributions from Si discs with different diameters. The Si discs were placed in water at a distance of 2 µm above the glass substrate. The diameters of the discs were 10, 20, 40, 60, and 80 µm and the thickness was 2 µm. The laser-induced heat was applied at the center of the disc with the heat density of 0.9 mW/µm^3, corresponding to the laser power of 60.4 mW. The laser spot size was 5 µm. **(A)** and **(B),** Cross-sectional images of the ΔT distributions at the time point of 1.2 ms normalized to **(A)** the maximum ΔT in each plot and **(B)** the maximum ΔT from the disc of 10 µm in diameter. Due to the high thermal conductivity of Si compared to water, the locally generated heat quickly spread out in the disc, and as a result, the temperature of disc decreased with the larger discs under the same laser power.
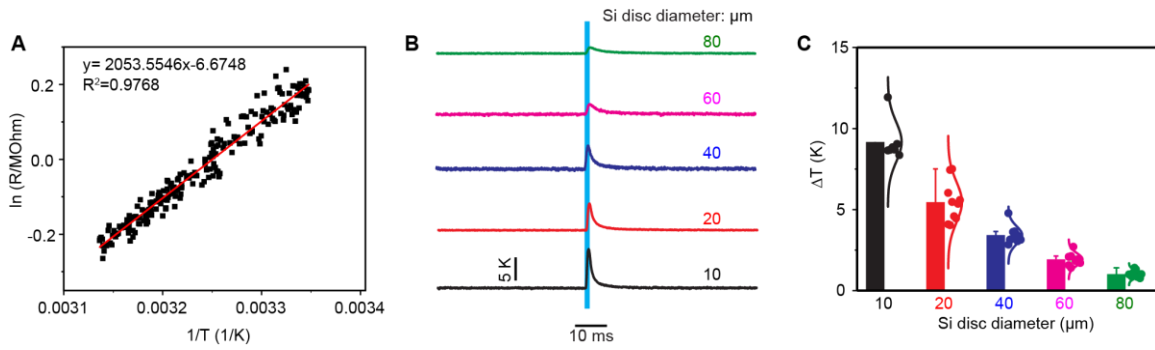
Fig. S25. The photothermal effect of the Si disc is inversely related to the disc size. **(A)** The pipette resistance over temperature curve calibrated from the micropipette for the later photothermal measurements. The temperature increase in the solution can then be inferred using the *T-R* calibration curve according to Yuanwen et. al. **(B)** Representative photothermal traces recorded from Si discs with different diameters under the same laser pulse profile (532 nm, 1 ms, ~61.4 mW, ~ 5 µm spot size). The cyan shaded area marks the light illumination period (1 ms). **(C)** Statistical analyses of the photothermal effect from Si discs with different sizes. *n*=7 for 10 µm; *n*=10 for 20 µm; *n*=10 for 40 µm; *n*=9 for 60 µm; *n*=10 for 80 µm.
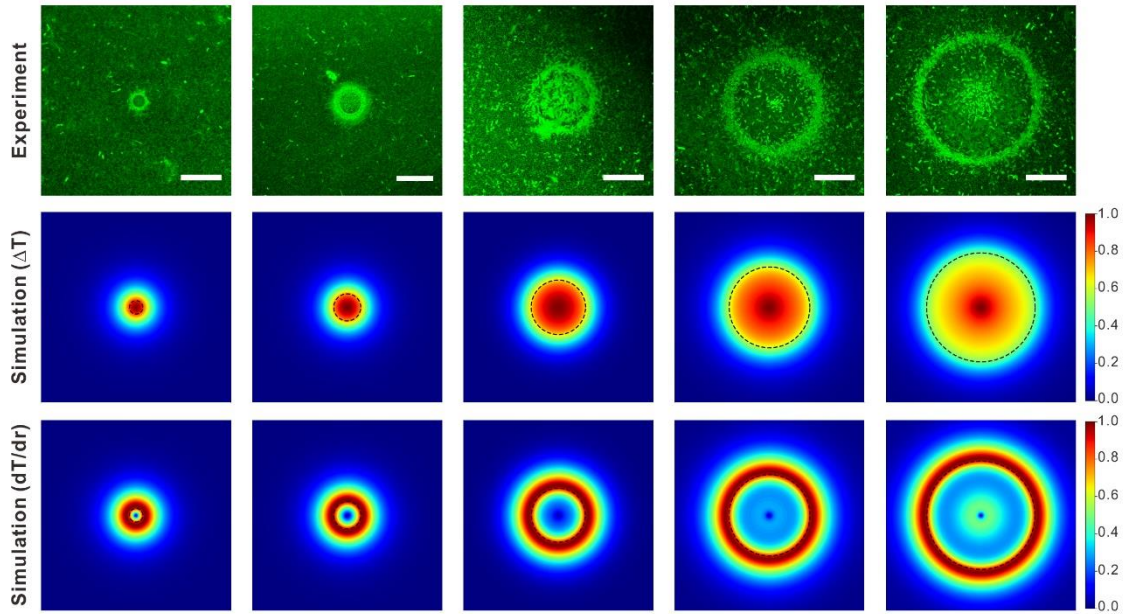
Fig. S26. The final calcium distribution patterns are correlated to the spatial temperature gradients right after the laser stimulation. The final calcium distributions (upper) were imaged after illuminating the centers of Si discs with the minimally required laser powers to elicit calcium signaling (592 nm, 1 ms, powers required for each disc are indicated in Fig. 3E). The results showed that for smaller Si discs (*e.g.,* 10 µm or 20 µm in diameter), the calcium hot spots were mostly outside the discs up to ~ 6 µm from the edges as opposed to be concentrated near the center. On the other hand, larger Si (*e.g.,* 60 µm or 80 µm in diameter) generated a bimodal calcium distribution with peaks near both the disc centers and the edges. Distributions of normalized absolute temperature change, *ΔT* (middle), and the normalized spatial temperature gradient, *dT/dr* (lower), were taken at 5 µm above the top of the disc at the time point of 1.2 ms with different disc diameters of 10, 20, 40, 60, and 80 µm. The laser-induced heat was applied at the center of the disc with the heat density of 4.82, 10.9, 19.3, 29.9, and 43.1 mW/µm^3 corresponding to the laser power of 3.62, 8.14, 14.4, 22.3, and 32.2 mW for the diameters of 10, 20, 40, 60, and 80 µm, respectively. Scale bar, 30 µm.
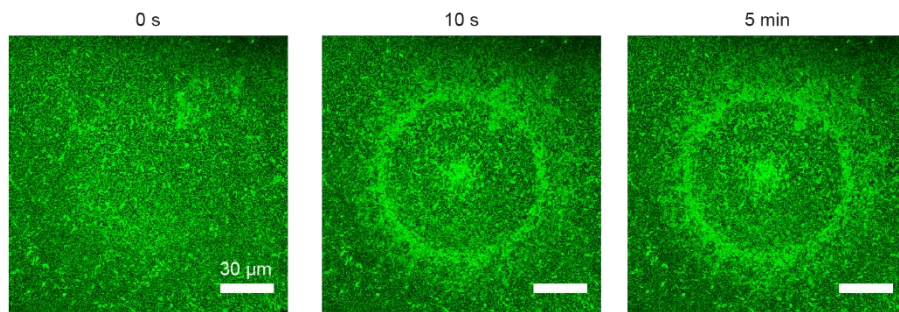
Fig. S27. The final calcium distribution pattern can be stable for at least 5 min. The final calcium fluorescence intensity distribution after illuminating a laser pulse (592 nm, 1 ms) at the center of the disc stays stable for least 5 mins.
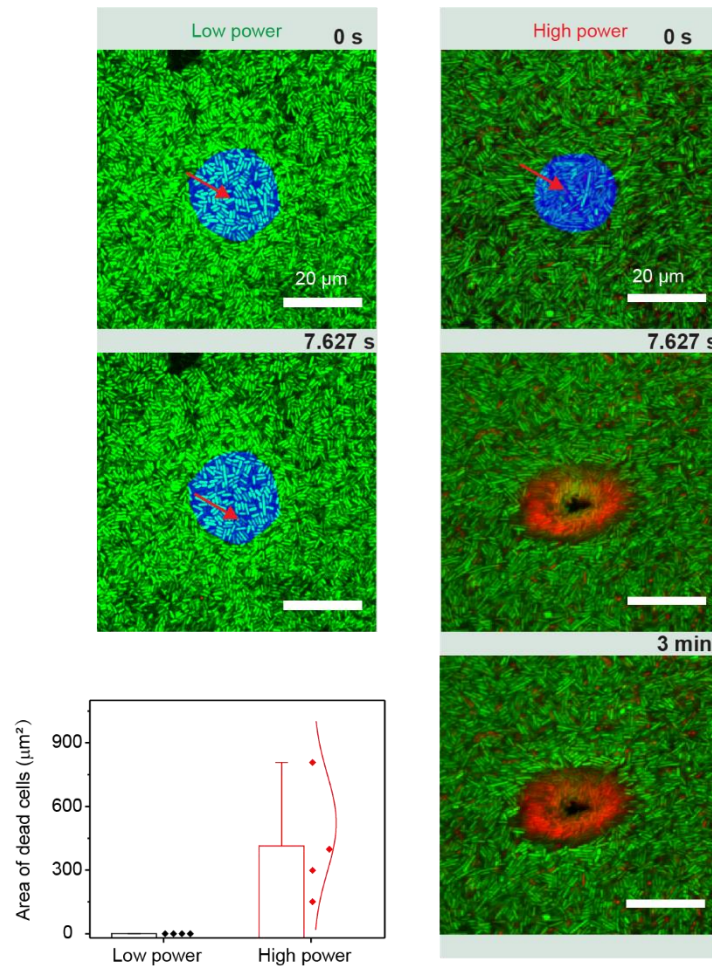
Fig. S28. LIVE/DEAD assays show the bacterial viabilities after laser illuminations on Si discs. After a low-power laser illumination (1-ms pulse of ~ 14.4 mW), *B. subtilis* biofilm cells around the disc stayed alive. After a high-power laser illumination (1-ms pulse of ~ 454.1 mW), the Si disc was kick off and the neighboring cells were dead. Quantitative analyses of the dead cell areas after both low- and high-power stimulations are provided.
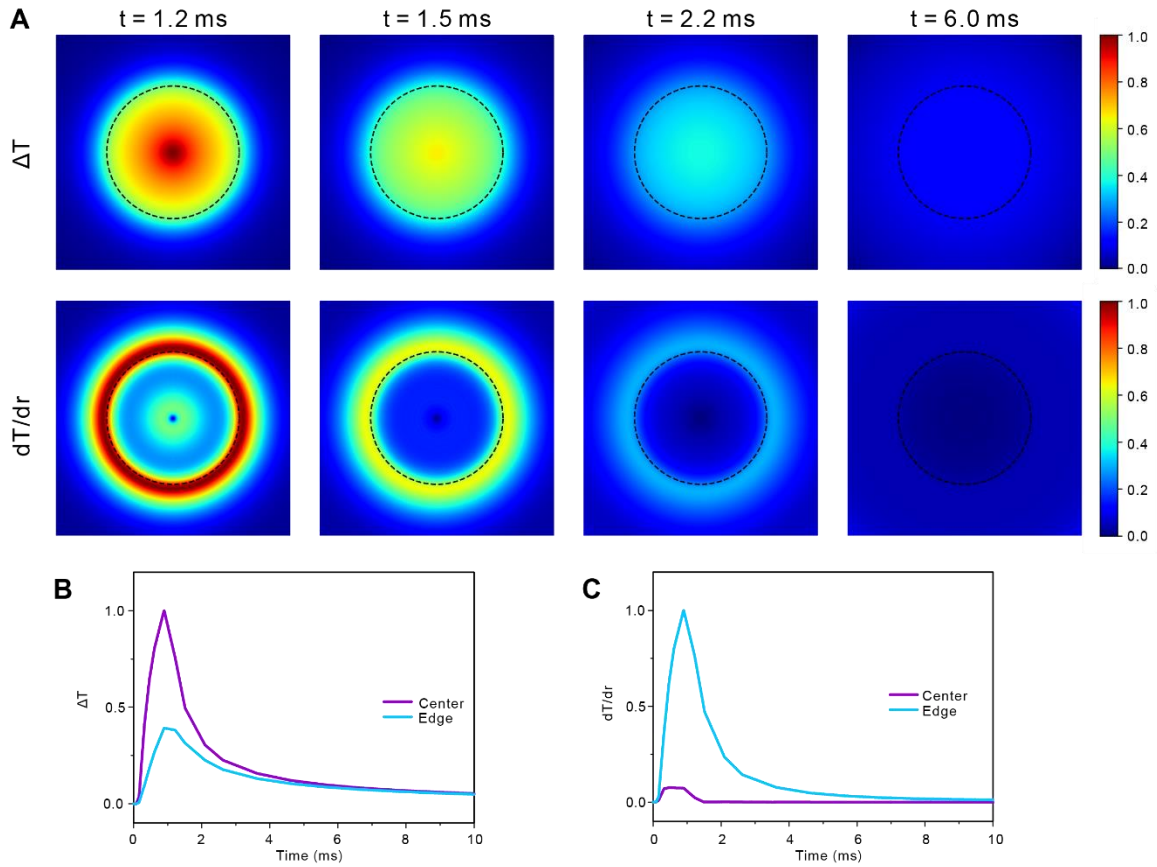
Fig. S29. The spatial temperature gradient is always peaked near the disc edge rather than the center. Time-lapse temperature distribution shows that the absolute temperature change (ΔT) was always higher near the disc center (**A** and **B,** diameter: 80 μm), while the spatial temperature gradient (dT/dr) was always higher near the disc edge (**A** and **C**).
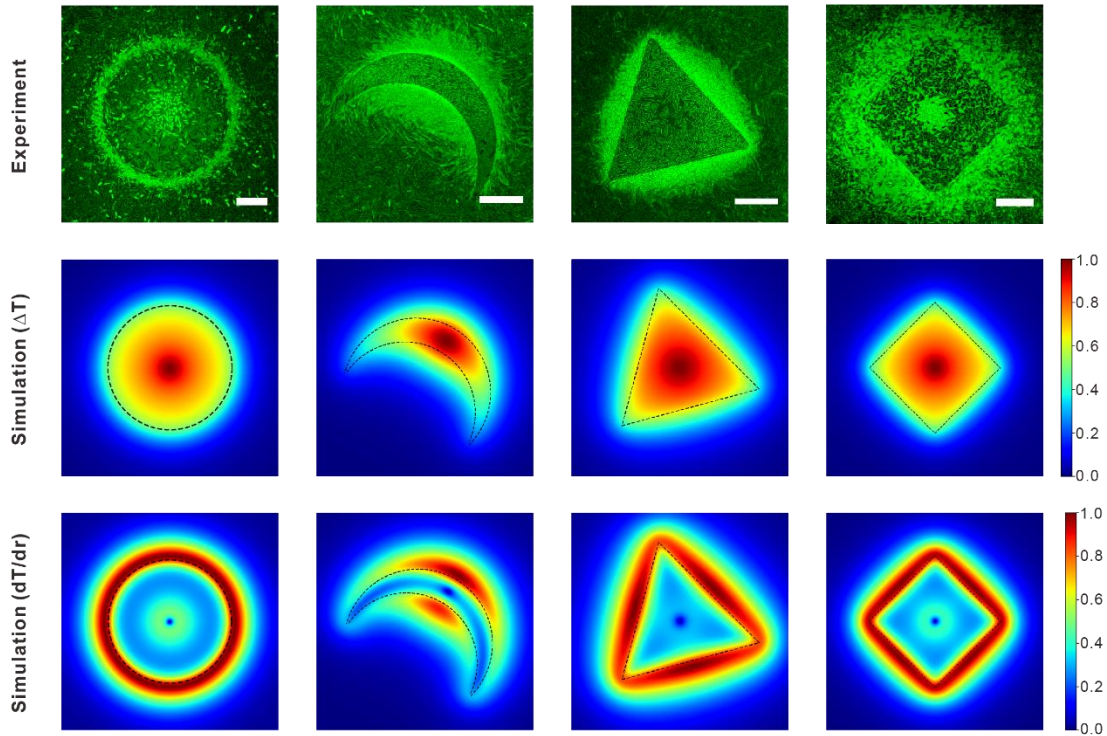
Fig. S30. Experimental and simulation results from Si micro-plates with different geometries further confirms the correlation between calcium distribution pattern and the spatial gradient of temperature. The final calcium fluorescence intensity distribution (upper) was imaged after illuminating a laser pulse (592 nm, 1 ms, disc, ~ 32.2 mW; crescent, ~32.2 mW; triangle: ~ 42.7 mW; Square: ~32.2 mW) at the center. The normalized absolute temperature change (ΔT) (middle, 1.2 ms after laser illumination) and spatial temperature gradient (dT/dr) (lower, 1.2 ms after laser illumination) were simulated by finite element analysis. Scale bar, 20 μm.
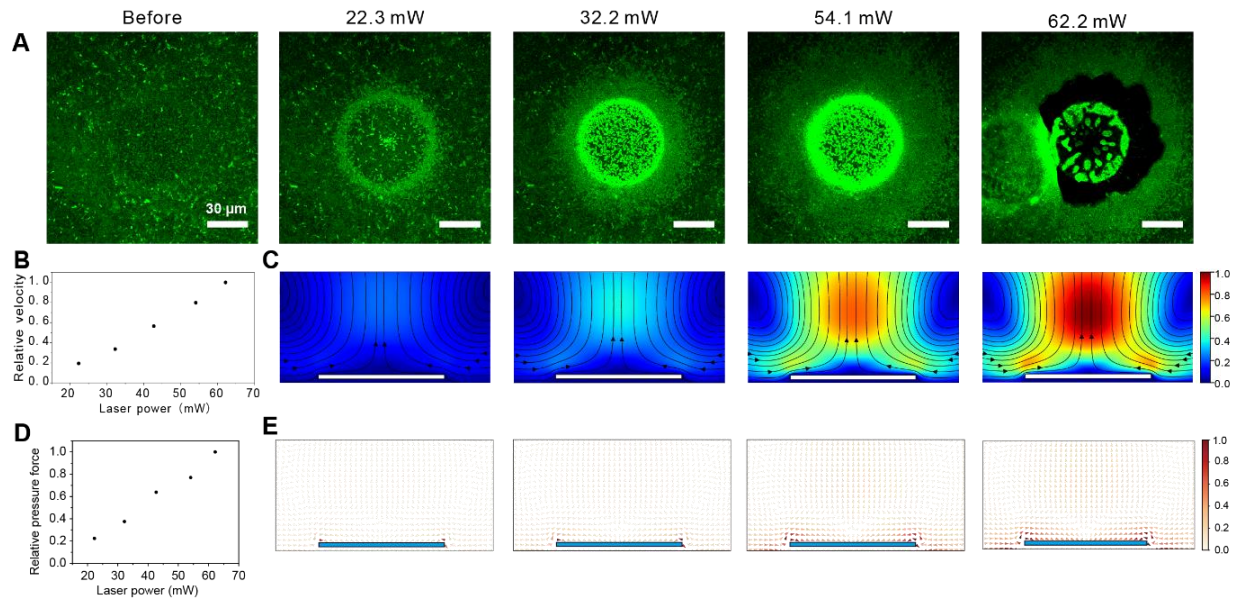
Fig. S31. Calcium signaling in conjunction with convective flows can cause biofilm disruption.
**(A)** Laser-power dependent calcium distributions show that both the intensity and area of the calcium fluorescence increased at higher laser powers until a threshold point where the Si disc (60 µm) was suddenly kicked away. A bimodal calcium distribution with peaks near both the disc centers and the edges was observed after the stimulation power of 22.3 mW (592 nm, 1 ms). With a higher power, cells that overlapped with the disc all got activated and calcium propagated far away from the edge of the disc. The Si disc was suddenly kicked away, and the biofilm broke simultaneously after stimulation at a power of 62.2 mW. Scale bar, 30 µm. **(B)** Plot of relative velocity normalized to the maximum fluidic flow velocity of the laser power of 62.2 mW. **(C)** Cross-sectional plots of the fluidic flow velocity distribution near the disc for the laser power of 22.3, 32.2, 54.1 and 62.2 mW, normalized to the maxium value from 62.2 mW. The color maps indicate the relative fluidic flow velocity while the arrows indicate the direction of the flow at the time point of 1.2 ms. The vertical convective fluidic flow was induced by the laser-induced heating, therefore, the fluidic flow (lateral direction) towards the heat source enhances as the laser power increases. Scale bar, 30 µm. **(D)** Plot of relative pressure force normalized to the maximum pressure force of the laser power of 62.2 mW, showing its dependency on the laser power. **(E)** The pressure force distribution near the disc for the laser powers of 22.3, 32.2, 54.1 and 62.2 mW at

the time point of 1.2 ms. The direction and color of arrows show the direction and the strength of the pressure force, respectively.
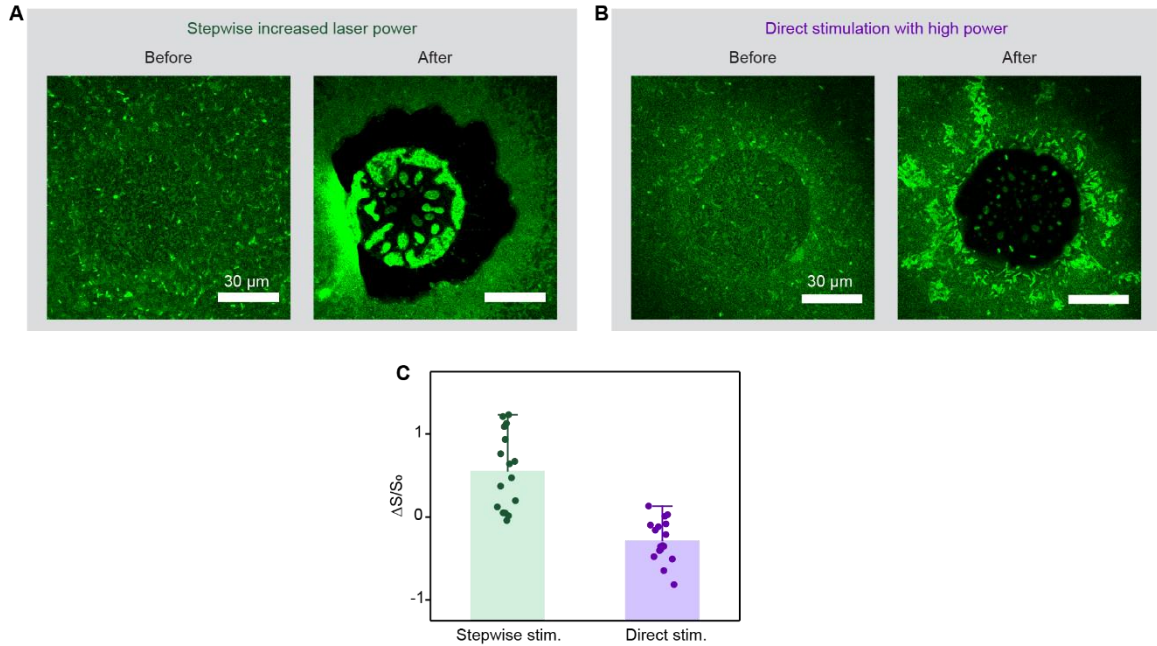
Fig. S32. Sequentially increased laser stimulations, compared to directly applying high-power laser stimulation, is more efficient to mechanically break the biofilm. Calcium distribution patterns and biofilms disruptions after sequentially applying increased simulation powers (**A**) and directly using a high power (**B**). In both cases, the final laser power applied to the biofilm was the same. However, compared to the sequentially increased laser stimulation, directly high-power laser simulation only yielded smaller areas of biofilm disruption. (**C**) Quantitative analysis of the disrupted biofilm areas in the non-overlapping regions versus the initial Si sizes. $n=16$ for the sequentially increased stimulation powers, $n=16$ for the direct stimulation with a higher power.
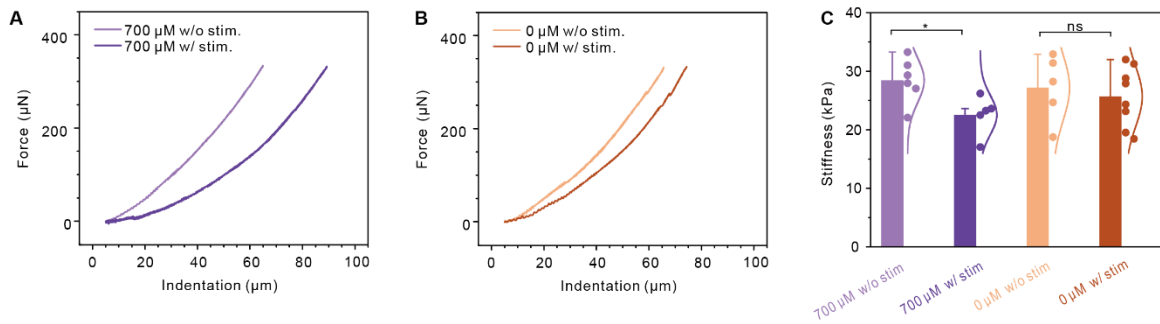
Fig. S33. Nanoindentation shows that the laser stimulation could alters the biofilm modulus.
(**A**) and (**B**) Representative force-indentation depth curves from two different spots (within the same biofilm) with and without laser simulation. The biofilms were cultured in normal Msgg agar medium contain 700 µM Ca^{2+} (**A**) or a modified Msgg medium without any Ca^{2+} (**B**). (**C**) Statistical analysis of the biofilm stiffness with and without laser stimulations. n=6 for the 700-µM Ca^{2+} cultured biofilm without stimulation; n=5 for the 700-µM Ca^{2+} cultured biofilm with stimulation; n=5 for the 0-µM Ca^{2+} cultured biofilm without stimulation; n=8 for the 0-µM Ca^{2+} cultured biofilm with stimulation. *, significant difference (p= 0.02); ns, no significant difference.
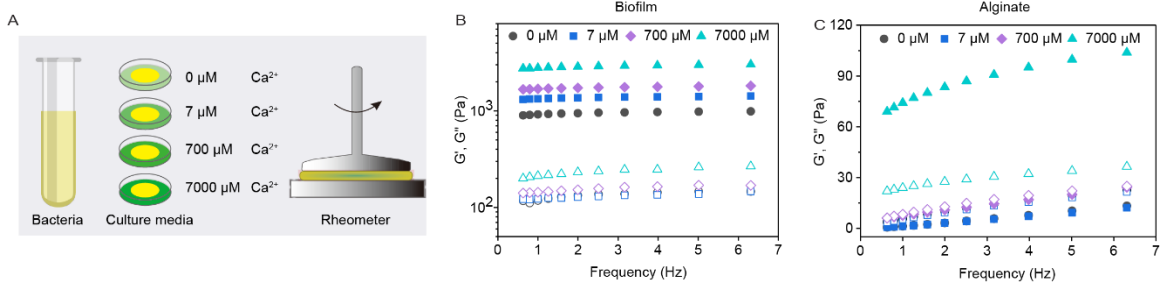
Fig. S34. Biofilms exhibit calcium-dependent mechanical properties, similar to alginate hydrogels that are ionically crosslinked by Ca²⁺. **(A)** Schematic illustration of biofilms inoculated from liquid medium and cultured in agar medium with various Ca^{2+} concentrations, followed by rheological measurements. **(B)** Comparison of rheological properties of biofilms cultured form Msgg agar medium with different concentrations of Ca^{2+}, measured by frequency sweep experiments (1% strain). **(C)** Comparison of rheological properties of 2% alginate gels crosslinked with different Ca^{2+} concentrations. The results show that the biofilm is also a viscoelastic material with a relatively higher storage modulus and relatively lower loss modulus, like a hydrogel system. Solid symbol: *G'*, storage modulus; Open symbol: *G''*, loss modulus.
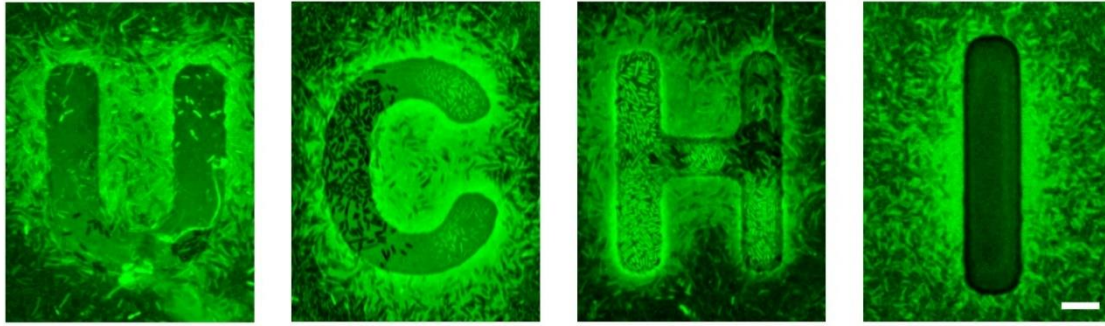
**Fig. S35. Ca^{2+} distributions in a living biofilm can be controlled by custom-design Si patterns.**

Scale bar, 10 µm.
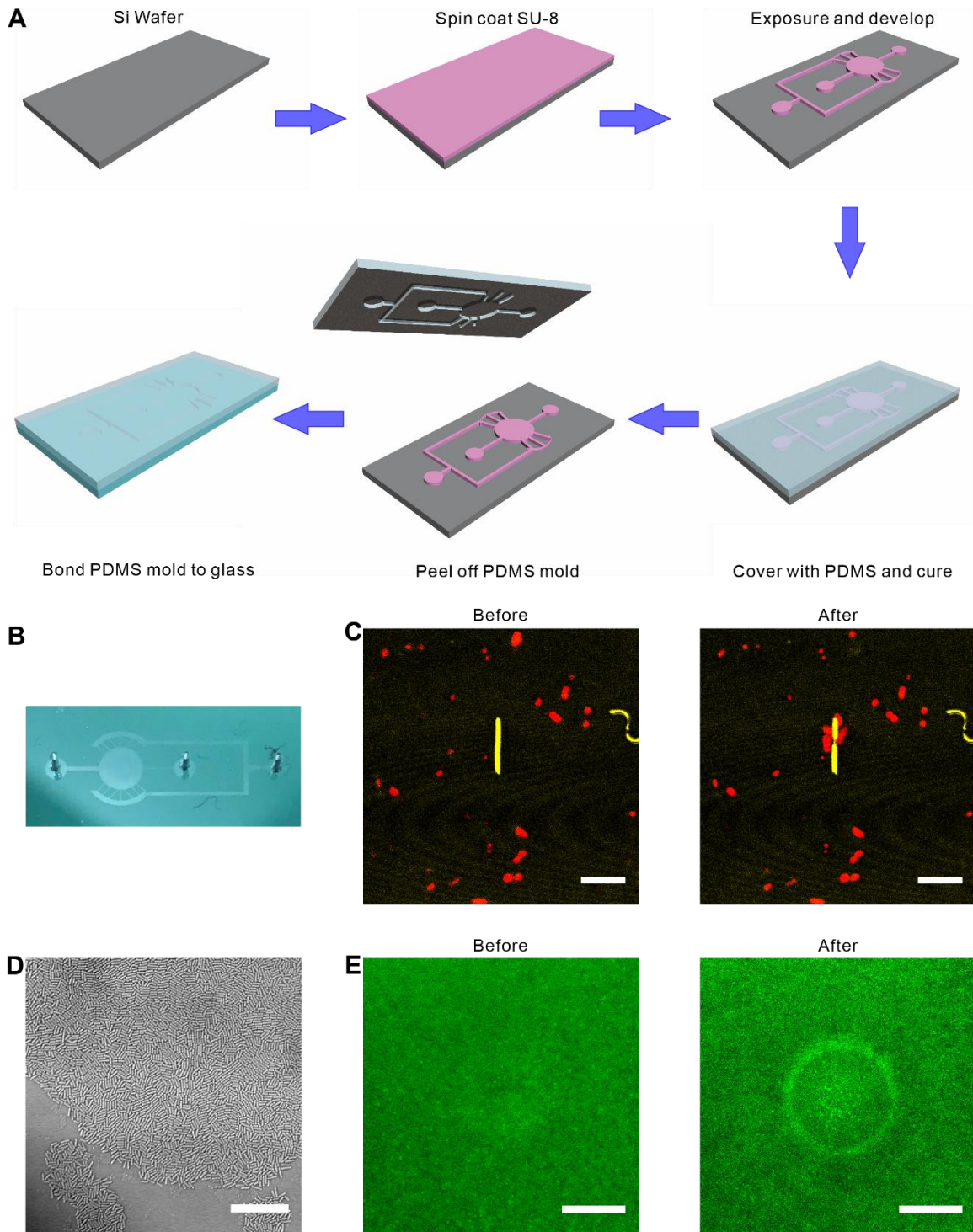
Fig. S36. Microfluidic system for cell attraction and single-layer biofilm stimulation experiments. (A) Schematic illustrations for the microfluidic device preparation. The fabrication involves standard photolithography, followed by soft lithography and replica molding. **(B)** An

optical image of the microfluidics device with two inlets (one for medium flow and the other for cell loading) and one outlet (for waste collection). **(C)** Si nanowires (yellow) can attract single cells (red) in the microfluidic device. Scale bar, 5 µm. **(D)** A microscope image of a monolayer biofilm cultured in the microfluidic chamber. Scale bar, 20 µm. **e,** Si discs can induce calcium dynamics of single-layer biofilm within the microfluidic channel. Scale bar, 30 µm.
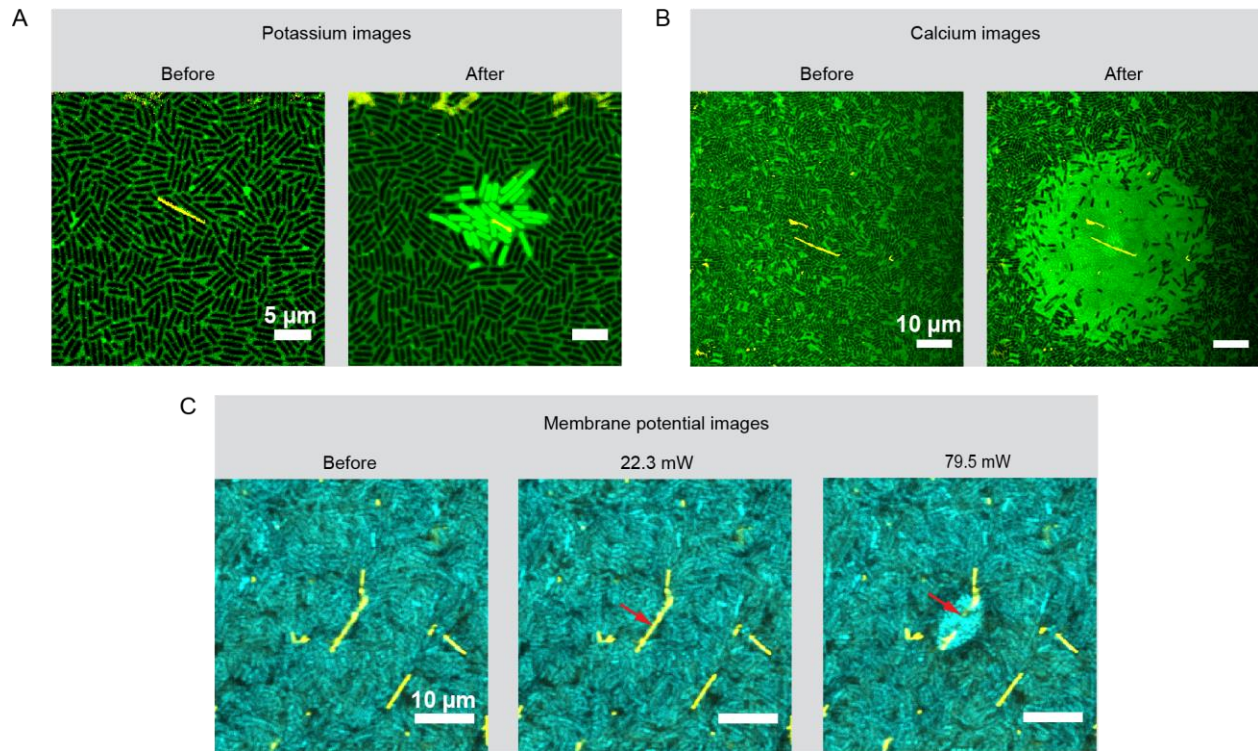
Fig. S37. Si nanowire can activate potassium, calcium and membrane signaling in *B. subtilis* biofilms. (A) A high-power laser pulse (592 nm, 1 ms, 79.5 mW) onto the Si nanowire can induce a potassium signaling in the biofilm. The biofilm was stained with 2 µM asante potassium green (APG)-2 AM. **(B)** A low-power laser pulse (592 nm, 1 ms, 22.3 mW) can induce a calcium signaling in the biofilm. The biofilm was stained with Fluo-4 AM. Compared to potassium signaling, calcium propagation required much lower power to be elicited. **(C)** A low-power laser pulse (22. 3 mW for calcium signaling) cannot induce any membrane potential changes in the biofilm while a high-power laser pulse (79.5 mW for potassium signaling) can cause local changes. The biofilm was stained with 10 µM Thioflavin T (ThT). Calcium signaling was not coupled with membrane potential change while the potassium dynamics may be correlated with the membrane potential.

Movie S1. Si nanowire can induce a rapid Ca²⁺ wave in *B. subtilis* biofilm. The biofilm was co-cultured with Si nanowires and the laser illumination (592 nm, ~22.3 mW, ~ 500 nm spot size) was on for 1 ms at the time point of 2.60 s. A fast Ca²⁺ wave propagation initiated from the bacteria cells near the nanowire under stimulation (left). Quantitative analysis of the fluorescence intensity of Ca²⁺ over time showing the immediate Ca²⁺ propagation (right).

Movie S2. Si nanowire induced Ca²⁺ signaling under inhibitor. The biofilm was co-cultured with Si nanowires and then stained with Fluo-4 (for calcium imaging),together with suramin (ATP receptor blocker). A laser illumination (592 nm, ~181.0 mW, ~ 500 nm spot size) was on for 1 ms at the time point of 2.60 s. Upon light illumination, only a small amount cells near the wire were activated. Simultaneously, we observed the biofilm underwent a mechanical stress that is visualized with biofilm vibration. While all the cells experienced a mechanical stress after light stimulation, most of the cell did not experienced an intracellular Ca²⁺ elevation. It suggests that mechanical stress cannot induce Ca²⁺ signaling in biofilm.

Movie S3. Large Si micro-disc induced a bidirectional circular Ca²⁺ wave in *B. subtilis* biofilm. The biofilm was co-cultured with the Si disc (80 µm diameter). A laser illumination (592 nm, ~32.2 mW, ~ 500 nm spot size) was on for 1 ms at the time point of 2.60 s. Upon light illumination at the center of the disc, cells near the disc edge first experienced intracellular elevation followed by bidirectional circular propagations towards the disc centroid and the biofilm outside the disc .

Movie S4. Calcium signaling in conjunction with convective flows can cause biofilm disruption. The biofilm was co-cultured with Si disc (60 µm diameter) and stimulated by stepwise increased laser power (**Supplementary Fig. S32**). After 3-times sequential increased laser power stimulation, the cells on and near disc experienced intracellular Ca²⁺ elevation and decreased extracellular Ca²⁺. The video showed that last laser illumination (592 nm, 62.2 mW) was on for 1 ms at the time point of 2.60 s. Upon laser stimulation, the Si disc was immediately kicked away, followed by biofilm disruption. Plus, the dispersal area in which the bacteria cells were stripped off biofilm was larger than disc area itself.